Sea-Ice Mapping of RADARSAT-2 Imagery by Integrating Spatial Contexture With Textural Features

Mingzhe Jiang, *Student Member, IEEE*, David A. Clausi, *Senior Member, IEEE*, and Linlin Xu, *Member, IEEE*

***Abstract*—Mapping different types of sea ice that form, grow, and melt in polar oceans is essential for shipping navigation, climate change modeling, and local community safety. Currently, ice charts are manually generated by analysts at the Canadian Ice Service based on dual-polarized RADARSAT-2/RADARSAT Constellation Mission imagery on a daily basis. Inspired by the demand for a computer-based mapping system, we have developed an automatic sea-ice classification method that integrates spatial contexture (unsupervised segmentation) with textural features (supervised pixel-level labeling). First, the full-scene image is oversegmented, and the segments are merged into homogeneous regions across the entire scene. Second, pixel-based classifiers (support vector machine and random forest) are compared for their ability to label the generated homogeneous regions. Finally, the segmentation and labeling are combined using a proposed energy function. The proposed method was tested on 18 dual-polarization RADARSAT-2 scenes acquired over the Beaufort Sea. This dataset contains water, young ice, first-year ice, and multiyear ice covering melt, summer, and freeze-up seasons. The proposed method obtains an average classification accuracy of 86.33% based on the leave-one-out validation. The experimental results show that the proposed method achieves promising classification results in both the quantity and quality measurements compared with benchmark methods. The robustness against incidence angle variance indicates that the proposed method is well qualified for operational sea-ice mapping.**

***Index Terms*—Classification, RADARSAT-2, random forest (RF), sea ice, segmentation, synthetic aperture radar (SAR).**

I. Introduction

THE interpretation of ice types and the analysis of their properties in polar ocean regions have several crucial applications, including the ship navigation, global climate monitoring, and animal migration forecasting [1], [2]. For the consideration of expense, efficiency, accuracy, and timing requirements, remote sensing has been chosen as an appropriate method for sea-ice monitoring. The satellite-based synthetic aperture radar (SAR) is the imaging system of choice for this application since it is not affected by cloud cover and, since self-illuminated, can be used equivalently under daytime or nighttime conditions. The Canadian Ice Service (CIS) actively performs ice mapping generation and interpretation daily. Skilled ice analysts process SAR images to generate ice charts that have defined geographical regions, known as "polygons," with an assigned "egg code" to each polygon defined by the World Meteorological Organization [3]. The egg code contains numerical codes that define ice concentration by the stage of development and floe size [4].

These ice charts have been used for decades but have limitations. First, egg codes are defined for large regions, so ice types are not identified at pixel resolution [5]. Second, polygons are generated subjectively. The results are affected by human bias, and there would be some variation between analysts. Third, the number of SAR scenes to be processed is expected to increase with time. CIS analysts used to process around ten scenes daily back to 2002 [6]. Nowadays, the manual interpretation of SAR imagery becomes very challenging due to the higher throughput required by the increasing data volume provided by the RADARSAT Constellation Mission [7] and Sentinel-1. Hence, manual procedures are potentially insufficient for future needs.

Therefore, an automated computer-based sea-ice mapping method is desirable. A suitable operational automated method should have the following characteristics:

1) the ability to generate ice maps that are consistent with expert interpretation;
2) the ability to classify different ice types as required for operational use on full-scene SAR imagery;
3) the ability to segment boundaries that match the natural ice and water boundaries;
4) the ability to be invariant to SAR sensor artifacts, such as banding noise and incidence angle variation.

However, mapping sea ice in SAR imagery is very challenging. First, different types of ice show very similar appearances in SAR imagery, especially when they are in contiguous development stages, such as young ice (YI) and first-year ice (FYI). Second, the ground truth is minimal. Supervised machine learning models rely on accurate pixel-level labels to achieve fair classification accuracy. However, ice charts released by primary national ice services only provide coarse labels for regions rather than pixels. Therefore, some studies prefer using samples selected from high-confidence regions for training and testing. Moreover, speckle noise and incidence angle variation can generate poor classification results. Boundaries between water and different types of ice, which are essential in sea-ice maps, can be degraded. Although many studies [8], [9] report high numerical classification accuracy,

Manuscript received 22 April 2022; revised 29 July 2022; accepted 6 September 2022. Date of publication 12 September 2022; date of current version 21 September 2022. This work was supported by the Natural Sciences and Engineering Research Council of Canada (NSERC) under Grant RGPIN-2017-04869, Grant DGDND-2017-00078, Grant RGPAS2017-50794, and Grant RGPIN-2019-06744. *(Corresponding author: Mingzhe Jiang.)*

The authors are with the Vision and Image Processing Research Group, Department of Systems Design Engineering, University of Waterloo, Waterloo ON N2L 3G1, Canada (e-mail: m63jiang@uwaterloo.ca; dclausi@uwaterloo.ca; linlinxu618@gmail.com).

Digital Object Identifier 10.1109/JSTARS.2022.3205849

the classification maps lack natural boundary information and suffer from speckle noise and interscan banding effect [10].

To address these challenges, we have developed and tested an automatic sea-ice mapping method. The following are the main contributions of this research.

1) We propose a novel sea-ice classification method by integrating segmentation with pixel-based labeling. The method not only adopts texture features for classification but also preserves critical boundaries between water and different ice types. Unlike most of the existing methods that only focus on improving numerical classification accuracy, the proposed method also aims to enhance the quality of classification maps.
2) To determine which classifier is more suitable for ice mapping, the performance of using support vector machine (SVM) and random forest (RF) in sea-ice classification is compared. The results demonstrate that RF achieves better overall accuracy compared to SVM. Since previous research has not sufficiently compared the performance of the popular RF and SVM classifiers for sea-ice classification, this benchmark would benefit other researchers for choosing the suitable classifier for their sea-ice monitoring tasks.
3) To evaluate the robustness of the proposed method, we compared the performances of the proposed method using SAR images with and without applying incidence angle correction. The experiment results indicate that the proposed iterative region growing with semantics (IRGS)-RF is more robust to incidence angle variance than pixelwise RF.
4) The system is validated on a full-scene dataset covering nine months (April to December), including melting, summer, and freezing seasons. The samples for validation are randomly selected across the full scene without any preferred regions. The experimental results demonstrate that the proposed method achieves accurate classification results in both quantity and quality.

To the best of our knowledge, this is the first work that combines unsupervised segmentation with supervised labeling for open water (OW) as well as multiple ice types and validated on a dataset that covers a whole year period. The rest of this article is organized as follows. Section II provides a review of studies done in sea-ice classification. The dataset used in this article is introduced in Section III. Section IV illuminates the steps of the proposed method. Section V presents the experimental results and analysis. Finally, Section VI concludes this article.

II. Background

Significant research has been published for exploring automated sea-ice mapping systems based on SAR data in the last decades. Early studies focused on modeling statistical distribution for ice types and water using backscattering intensity. Scheuchl et al. [11] explored the potential of using cross-polarization SAR imagery to monitor sea ice. The higher information content from dual-polarization data showed the capability for developing an automated sea-ice classification system. Ward et al. [12] modeled the characteristics of ice and water using a mixture distribution. However, several studies concluded that only using backscatter intensity is insufficient in distinguishing different ice types [13], [14]. Therefore, many researchers turned to polarimetric SAR data since they hold more information separating different ice categories. Gill and Yackel [15] exploited the polarimetric parameters derived by decomposition algorithms with the maximum likelihood classifier to categorize different types of FYI. By extracting matrix-invariant-based features from fully polarimetric ALOS-2 (L-band), Radarsat-2 (C-band), and TerraSAR-X (X-band) data, Singha et al. [16] separated water from sea ice with 100% accuracy.

Research has shown the potential of using quad-polarization SAR data for successful scene classification [15], [16], [17]. Nevertheless, the quad-polarization scene is not used operationally because of its narrow swaths. In contrast, dual-polarization data have been demonstrated to be a reliable source for sea-ice–water classification when combined with textural features and machine learning methods. Many features have been explored for sea-ice classification, e.g., Shannon entropy [18], local binary patterns [19], and cross-correlation between different polarizations [20]. A popular method for texture feature extraction from SAR sea-ice images is the gray-level co-occurrence matrix (GLCM) [21]. Clausi [22] analyzed the relation between gray-level quantization and classification accuracy using the GLCM features. The study suggested that using contrast, entropy, and correlation with a quantization level of 64 is sufficient for classifying sea ice. Liu et al. [23] extracted GLCM features for segmentation and implemented an SVM to discriminate ice from water. Su et al. [24] combined surface temperature and GLCM features from the Moderate Resolution Imaging Spectroradiometer images to train an SVM model for ice–water classification. Tan [25] proposed a semiautomated ice mapping method and obtained a good identification for water.

Besides investigating different features, several studies have explored sea-ice classification using SAR imagery obtained at different working frequencies. Mahmud et al. [26] collected SAR data acquired from ALOS PALSAR (L-band), RADARSAT-2 (C-band), and QuikSCAT (Ku-band) to classify landfast FYI and multiyear ice (MYI) in the Arctic. The results indicated that L-band performed better for FYI, whereas C-band is robust to distinguish MYI. Given the longer wavelength, L-band can detect the ice underneath melting ponds and wet snow in the melting season because of the enhanced penetration capability [27]. C-band is a better choice to monitor ice in the cold and dry winter since it provides details of surface roughness with higher resolution [28], [29].

To distinguish ice types, many classification models have been used, including the Bayesian classifier [30], [31], SVM [32], decision trees [33], and RF [34], [35]. With the rapid development of graphics processing unit in the past decade, deep learning has been applied to remote sensing [36]. Ressel et al. [37] extracted GLCM-based textural features from TerraSAR-X imagery and fed them to a neural network and classified three different ice types. Song et al. [38] combined a residual convolutional neural network with long short-term memory units to learn spatial and temporal features for sea ice. Khaleghian et al. [8] compared the performance of several popular deep learning architectures for sea-ice classification using Sentinel-1 data.

The studies mentioned above did achieve reasonable results. However, none of them has been deployed for operational sea-ice classification for the following reasons. First, deep learning models usually perform inference on image patches rather than whole images. The patch size constrains the receptive field. A small patch size might provide insufficient characteristics for classification, while a large window size might contain different ice types and contaminate the information extracted. Thus, classification maps produced by pixelwise deep learning models are usually contaminated by noise [39], [40]. Moreover, boundaries between ice and water can be smudged because of the inhomogeneity of the patch [41]. Similarly, GLCM features, since they depend on fixed sized windows, also generate segmentation errors at class boundaries [42]. The defective classification result caused by this drawback is demonstrated and discussed in Section V. Second, supervised machine learning methods require many reliable pixel-level labeled samples for training and testing. Since leading national agencies, such as CIS, the Norwegian Ice Service, and the Russian Arctic and Antarctic Research Institute, do not provide pixel-level ice charts, applying deep learning methods for operational use is not feasible at this time. Applying traditional machine learning methods with limited labeled samples has led to only training and validating on particular regions or sample points rather than full scenes [43], [44], [45].

As only using pixelwise classifiers usually leads to poor-labeled sea-ice classification maps [46], some researchers tried to refine the pixelwise results to more visually appealing ice maps. Ochilov and Clausi [47] built a Markov random field with maximum *a priori* estimation for ice–water classification. Zhu et al. [43] first classified sea ice into five categories based on SVM. Then, a conditional random field (CRF) was applied to the original result as postprocessing. Leigh et al. [48] combined spatial and contextual features by modeling a CRF using a pixel-based classifier for ice–water classification.

This study aims to explore the operational sea-ice mapping system. Inspired by the idea of producing detailed sea-ice maps with high accuracy and natural boundaries to meet the operational requirements, we have designed and implemented an automated sea-ice mapping system that combines unsupervised segmentation with supervised labeling. One of the challenges for sea-ice mapping is the SAR incidence angle effect [49]. Some studies [50], [51] consider utilizing SAR incidence angle as one of the features to refine classification accuracy. In this article, we did not aim to directly solve the incidence angle effect using incidence angle normalization/correction. However, we note that the region-based segmentation approach adopted in this article is effective in mitigating its adverse effects. Furthermore, the texture-based features adopted in this study are robust to incidence angle variation [52]. More details are elaborated in Section IV.

III. Dataset Used in the Study

The dataset we used to validate our algorithm is a subset of the dataset of Leigh et al. [48] used for ice–water classification. The original dataset contains 20 scenes acquired by C-band RADARSAT-2 SAR satellite under dual-polarized (HH and HV) ScanSAR wide beam mode. Owing to the lack of detailed ice charts, only 18 scenes are selected for ice types mapping in this article. The date of capture for each scene is listed in Table I. The dataset was acquired in the year 2010 at overlapping regions over the Beaufort Sea. Fig. 1 displays the geographical location of the dataset . The nominal pixel spacing is 50 by 50 m, and the image dimension is around 11 000 by 10 000, which represents the largest range size produced by RADARSAT-2. The coverage of each scene is 500 km in both azimuth and range. The incidence angle varies from 20° to 49° in both the ascending and descending orbits. The dataset was acquired from April to December, which contained melt and freeze-up seasons, the most challenging times of the year. Sea-ice conditions from January through March are more stable and less important for operational purposes, as well as less challenging for scene classification. Therefore, the dataset does not contain this period.

TABLE I
Dataset Used in This Study

Scene ID	Date of capture	Orbit	IA (°)
20100418	20100418 16:33:15	D	19.72 to 49.46
20100426	20100426 04:04:39	A	19.55 to 49.44
20100510	20100510 03:56:20	A	19.58 to 49.44
20100524	20100524 03:47:56	A	19.61 to 49.46
20100623	20100623 04:12:55	A	19.63 to 49.45
20100629	20100629 16:33:26	D	19.71 to 49.43
20100721	20100721 17:32:08	D	19.64 to 49.47
20100730	20100730 16:29:08	D	19.61 to 49.46
20100807	20100807 17:36:10	D	19.77 to 49.47
20100816	20100816 16:33:29	D	19.74 to 49.45
20100907	20100907 03:56:14	A	19.59 to 49.44
20100909	20100909 16:33:21	D	19.63 to 49.48
20101003	20101003 16:33:24	D	19.59 to 49.46
20101021	20101021 04:13:25	A	19.50 to 49.43
20101027	20101027 02:57:26	A	19.58 to 49.43
20101114	20101114 04:13:04	A	19.57 to 49.43
20101206	20101206 01:51:39	A	19.59 to 49.39
20101214	20101214 02:57:25	A	19.58 to 49.45

The date of capture, satellite orbit: descending (D)/ascending (A), and incidence angle (IA) range are included.

We downsample the original images using a four-by-four window for average pooling to reduce the computational cost and processing time. Although the pixel resolution reduces to 200 m after the downsampling, it still provides a substantially more detailed ice map than human interpretation.

In this study, we focus on classifying OW, YI, FYI, and MYI in SAR imagery [53]. An example scene from the dataset is shown in Fig. 2, which is acquired on April 26, 2010. This scene is quite complicated with the appearance of different types of ice (FYI and MYI) and land. The backscatter decreases from right to left due to the incidence angle effect. The HV scene has a lower signal-to-noise ratio and is darker compared with the HH scene.

For training and testing purposes, we randomly labeled 500 sample pixels per scene for all 18 scenes. These sample points are used to train the classifiers and validate the performance. An example of a scene with labeled sample points is shown in Fig. 2(d). The scene is covered by FYI (yellow) and MYI (red). In order to produce an appropriate dataset for training and testing, all the labeled samples are randomly selected across the whole scene without any preferred region.

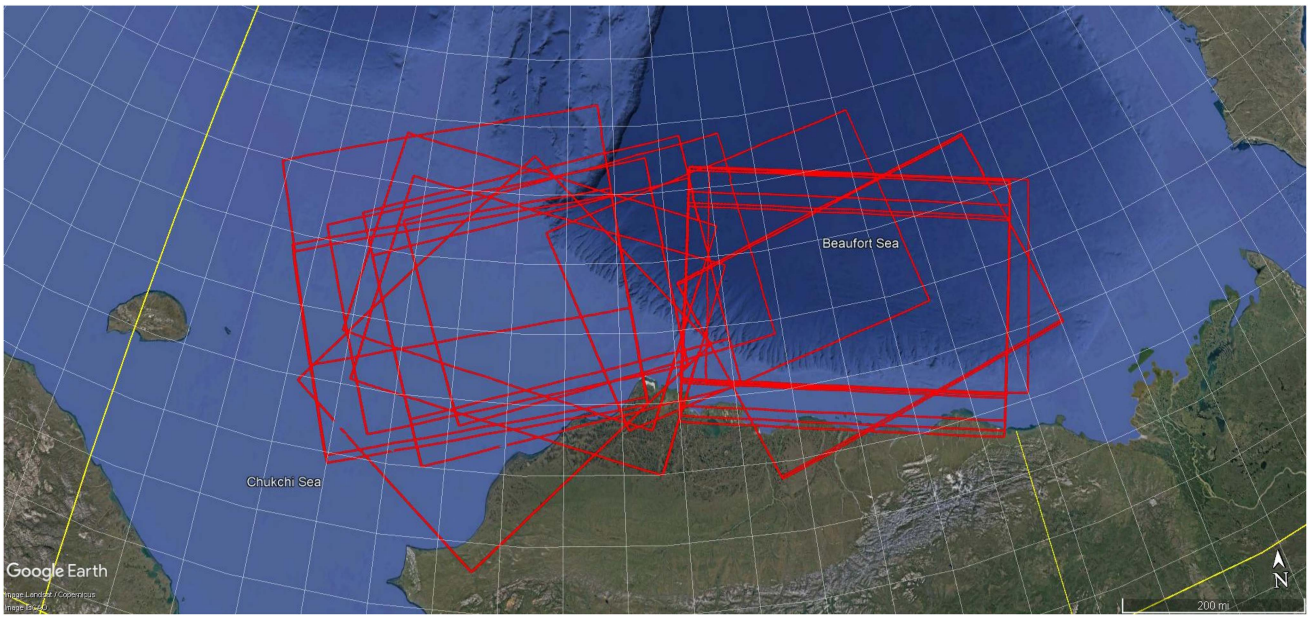

Fig. 1. Location of the 18 scenes in the Beaufort Sea.

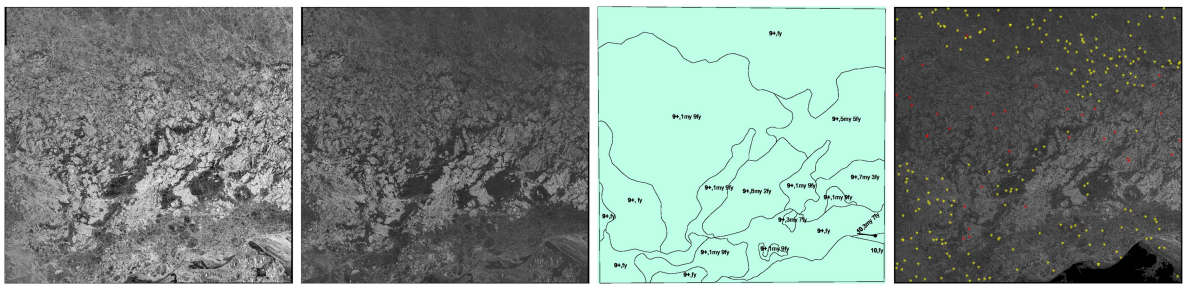

(a) (b) (c) (d)

Fig. 2. Example scene captured on April 26, 2010 (Scene ID: 20100426_040439). (a) HH polarization. (b) HV polarization. (c) Reference ice chart. (d) 500 sample points selected for training and test (Yellow: FYI. Red: MYI).

IV. Methodology

A. Problem Formulation

Let Y denote the SAR image that consists of N pixels, i.e., $Y = \{y_i | i = 1, 2, \ldots, N\}$ and L is the associated label map $L = \{l_i | i = 1, 2, \ldots, N\}$ that consists of a total of K classes of different ice types, where $l = \{1, 2, \ldots, K\}$. Sea-ice mapping from SAR image aims to estimate L given Y.

Algorithmically, first, Y is segmented into a total of T homogeneous regions $Y = \{R_1, R_2, \ldots, R_T\}$, where R_r consists of n_r pixels

$$R_r = \{y_i^r | i = 1, 2, \ldots, n_r\}. \quad (1)$$

To estimate the label of R_r, denoted by l_{R_r}, the label of each pixel, i.e., $\{l_{y_i} | i = 1, 2, \ldots, n_r\}$, in R_r is estimated. Then, $\{l_{y_i}\}$ is used to derive the label of the region l_{R_r} via the proposed energy function.

The proposed classification system consists of two main components shown in Fig. 3. The system uses HH and HV polarized images of the scene, a pretrained pixelwise classifier, and an optional landmask file as inputs. The left block in the flowchart is the IRGS segmentation [54] to generate $Y = \{R_1, R_2, \ldots, R_T\}$, and the right block is the pixelwise labeling to determine l_{y_i}. Details are described in the following subsections.

B. Unsupervised Segmentation

Operational SAR imagery used for sea-ice mapping at CIS has large extents. The gradual change of incidence angle from near range to far range leads to a corresponding change in within-class backscatter. Therefore, a two-step segmentation strategy called "glocal," shown in Fig. 3, was introduced to suppress the incidence angle effect [48]. First, the whole scene is segmented into subregions called "autopolygons" [55] using a modified watershed algorithm [56]. Only the HV scene is used in this step, which is shown in Fig. 4(a), because it is less sensitive to both incidence angle variation and surface roughness caused by winds [57].

Within each autopolygon, an IRGS segmentation is performed using the HH and HV polarized images. This step is presented in

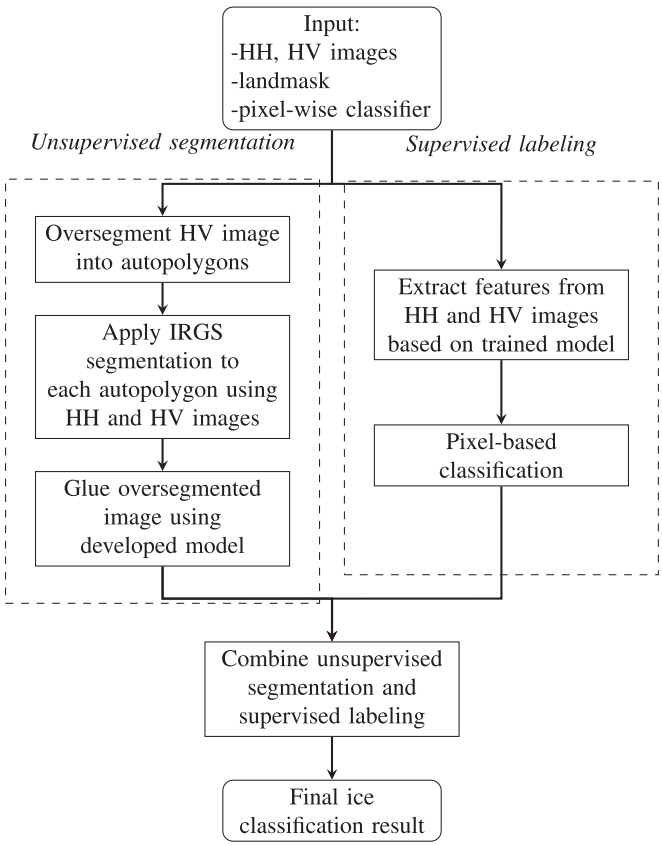

Fig. 3. Flowchart of the ice mapping system. Inputs are HH/HV images, landmask (optional), and a trained classifier (SVM or RF). The left block calculates contextual information by the unsupervised segmentation, while the textural feature is extracted in the right block. Then, these features are combined using the proposed energy function to generate the final classification map.

Fig. 4(b). Each region in an autopolygon results from oversegmention and is regarded as a node in a region adjacency graph. Since each node is homogeneous and only contains water or one ice type, an arbitrary label is assigned to each region for further processing. This is the local step of the unsupervised segmentation. The effects of speckle noise and incidence angle are restrained by processing each autopolygon individually.

The second step is called "global." Once the oversegmented result is available, a gluing step is operated across the whole image. The edge strength and statistical information from HH and HV polarization are considered during this merging step. The final segmentation result contains six classes with arbitrary labels. This method is called "glocal" as it combines local oversegmention and global merging.

The structure of IRGS segmentation is elucidated in [58]. Each autopolygon is segmented into four clusters, and the clusters are merged into six classes in the global step. The following parameters are applied to the segmentation for all the scenes in the dataset. β_1 and β_2 used for estimating multilevel logistic model are 3 and 0.4, respectively. The number of iterations is set to 100 to achieve an oversegmented result. According to previous experiment results, the values of β_1 and β_2 have little impact on the final oversegmentation results when the iteration reaches 100.

TABLE II
GLCM PARAMETERS USED IN THE STUDY

Window size (pixels)	Spatial distance (pixels)
5 × 5	1
11 × 11	1
25 × 25	1
25 × 25	5
51 × 51	5
51 × 51	10
51 × 51	20
101 × 101	10
101 × 101	20

C. Supervised Labeling

1) Features: The following GLCM features [59] are selected to build the automated sea-ice classification model in this study:

1) angular second moment (ASM);
2) contrast (CON);
3) correlation (COR);
4) dissimilarity (DIS);
5) entropy (ENT);
6) homogeneity (HOM);
7) inverse moment (INV);
8) mean (MU);
9) standard deviation (STD).

The choice of window and step size of GLCM features can impact the performance of sea-ice classification. The window size determines the perceptive area for textural feature extraction. For instance, a small window usually works for distinguishing OW since calm water surface has less texture in contrast to different types of sea ice. Small window sizes also work better to detect textural features from within leads and floes, while the complex repeating patents caused by fissures and cracks in different ice types require larger window sizes to capture. The spatial distance of GLCM features determines the scale of repeating patterns. For example, FYI has more dense repeating patterns compared with MYI. The chosen window and step sizes of GLCM features are listed in Table II. In addition to the 162 GLCM features, we add individual pixel intensity, local average, and maximum pixel intensities in 5 × 5 and 25 × 25 windows. All the features are extracted from HH and HV polarized scenes, resulting in a set of 172 features [48].

In order to minimize computation time and to minimize the "curse of dimensionality" [60], [61], a feature search was performed to reduce the number of features. Recursive feature elimination with cross validation [62] is applied to select the best feature combination in this study. The feature with the least importance is discarded in each iteration. The process is repeated until the best feature combination is found. Since the dataset used in this article consists of 18 scenes, the feature search is deployed with a cross-validation strategy. The feature search executes 18 times. In each loop, a feature importance estimator is trained on the 17 scenes and tested on the remaining scene to determine the importance of each feature. This procedure was carried out 18 times, and each scene has enrolled in both training and test sets. This cross-validation strategy is called leave-one-out (LOO). After the LOO is performed, the feature

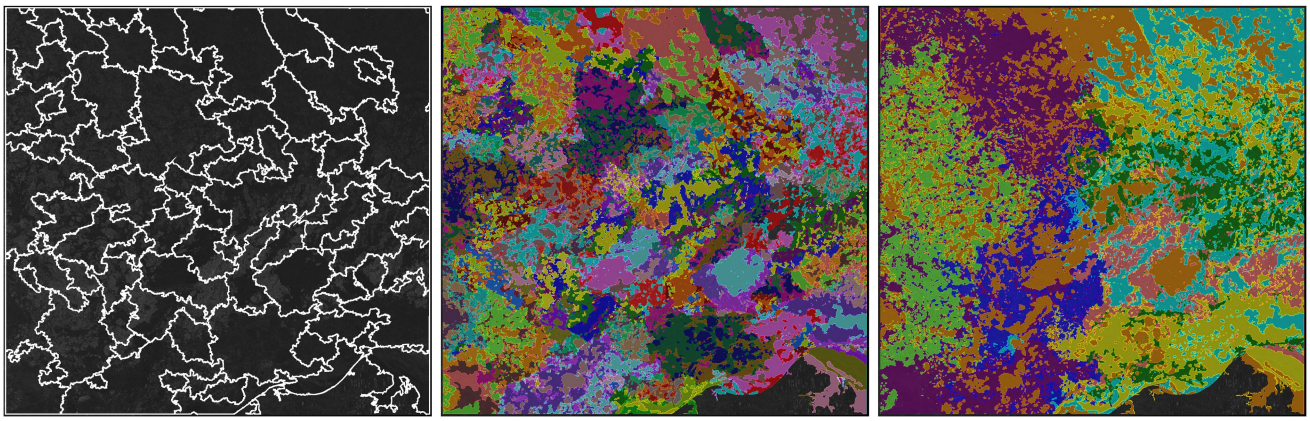

(a) (b) (c)

Fig. 4. IRGS result for April 26, 2010 (scene ID 20100426). (a) Autopolygons generated by the modified watershed algorithm. (b) Local oversegmentation result. (c) Glocal results.

TABLE III
LIST OF SELECTED 30 FEATURES USING RFE AND CROSS-VALIDATED SCHEME

#	Polarization	Feature Type	Window size	Step size
1	HH	Pixel Intensity	N/A	N/A
2	HV	Pixel Intensity	N/A	N/A
3	HV	GLCM MU	11 × 11	1
4	HH	GLCM COR	25 × 25	1
5	HH	GLCM MU	25 × 25	1
6	HV	GLCM MU	25 × 25	1
7	HH	GLCM MU	25 × 25	5
8	HV	GLCM MU	25 × 25	5
9	HH	GLCM MU	51 × 51	5
10	HV	GLCM ASM	51 × 51	5
11	HV	GLCM HOM	51 × 51	5
12	HV	GLCM MU	51 × 51	5
13	HH	GLCM MU	51 × 51	10
14	HV	GLCM ASM	51 × 51	10
15	HV	GLCM MU	51 × 51	10
16	HH	GLCM MU	51 × 51	20
17	HV	GLCM ASM	51 × 51	20
18	HH	GLCM DIS	101 × 101	10
19	HH	GLCM INV	101 × 101	10
20	HH	GLCM MU	101 × 101	10
21	HV	GLCM ASM	101 × 101	10
22	HV	GLCM HOM	101 × 101	10
23	HV	GLCM INV	101 × 101	10
24	HV	GLCM MU	101 × 101	10
25	HH	GLCM CON	101 × 101	20
26	HH	GLCM MU	101 × 101	20
27	HV	GLCM ASM	101 × 101	20
28	HV	GLCM HOM	101 × 101	20
29	HV	GLCM INV	101 × 101	20
30	HV	Pixel Average	25 × 25	N/A

importances from each iteration are summed up to calculate the final feature ranking. After running the feature search, the 30 most important features are selected. The result is listed in Table III.

An appropriate classifier is crucial for a classification task. Xu et al. [63] compared the performance of different classification techniques (SVM, artificial neural network, decision trees, generalized additive model, and penalized linear discriminant analysis) using RADARSAT-1 imagery. In their study, tree-based classifiers and SVM achieved better performance than the others. Therefore, RF and SVM were chosen as the labeling methods in our study.

2) Support Vector Machine: An SVM is a supervised learning model for classification and regression. The object of SVM is to calculate a linear hyperplane in the feature space to separate data from different classes. Only a subset of the training samples called support vectors, are chosen to determine the hyperplane. The hyperplane maximize the margin to the support vectors is selected as the decision boundary. The training process of SVM is to minimize the following loss function:

$$\left[\frac{1}{n}\sum_{i=1}^{n}\max\left(0, 1-y_i\left(\mathbf{w}^T\mathbf{x}_i-b\right)\right)\right]+\lambda\left\|\mathbf{w}\right\|^2 \quad (2)$$

where $\mathbf{w}$ and b are parameters for the hyperplane. y_i are class labels $\in \{1, 2, 3, 4\}$. YI, FYI, MYI, and water are assigned labels 1, 2, 3, and 4, respectively. The original max-margin SVM only works with linearly separable data. However, the tasks in the real world are usually non-linear separable. Therefore, a kernel function is applied to map data from low feature dimensions to higher feature dimensions for linear separability. Polynomial, radial basis function (RBF), and sigmoid are the most popular nonlinear kernel function. The RBF kernel is applied for SVM in this article with the form

$$K\left(\overline{t_i}, \overline{t}\right)=\exp\left(-\gamma\left|\overline{t_i}-\overline{t}\right|^2\right) \quad (3)$$

where γ is a Gaussian parameter for sample scaling. RBF kernel projects samples to high-dimensional feature space and makes them separable. $\overline{t_i}$ and $\overline{t}$ are two samples, and the similarity is measured in Euclidean distance. Since the decision boundary of SVM is computed based on a few support vectors, it requires less memory and computational power. Fewer support vectors also help to reduce the overfitting in training. Moreover, SVM is versatile with different kernel functions for various classification. missions [64].

3) Random Forest: RF [65] is an ensemble learning model for classification and regression. It is an aggregation of diversified decision trees binding by bootstrap aggregating (bagging) strategy. The key idea of RF is random—both samples and

features are selected to train the decision trees and their nodes. Each decision tree is trained by a subset of the whole dataset using bootstrap sampling, and the node of the tree is grown from a random feature of the input data. This learning method averages the learned weights for all the features and helps to prevent overfitting problems. The bagging method makes the classifier tolerate the noise appearing in the dataset, which is crucial for our research since SAR images are contaminated by speckle noise. The aggregation of decision trees can be trained by parallel computing and reduce the training and testing time [66]. In contrast to SVM, RF does not require feature searching since features are randomly selected, and the importance is assigned to each feature using GINI index [67]. The hyperparameters of RF are determined by utilizing cross-validation-based grid searching. The search range for the number of trees is $\in \{25 \rightarrow 500 \mid \text{step} = 10\}$, max depth is $\in \{2 \rightarrow 20 \mid \text{step} = 2\}$, and minimum samples per leaf is $\in \{1 \rightarrow 10 \mid \text{step} = 1\}$. The best combination of hyperparameters determined by grid search is: the number of trees $= 200$, max depth $= 12$, and minimum samples per leaf $= 2$. In order to evaluate the performance of SVM and RF using the same feature set, RF is trained on the selected features in this article.

In this study, SVM and RF are deployed as pixelwise classifiers for the following reasons. First, both the models have been applied for remote sensing tasks, and the results are promising according to previous studies. Second, SVM and RF have their own techniques to suppress overfitting and increase robustness. Finally, the runtime for predicting each scene is less than 30 min, which is acceptable for operational use.

D. Combination of Segmentation and Labeling

By performing the unsupervised segmentation algorithm, $Y = \{R_1, R_2, \ldots, R_T\}$ is determined. Each R_r in Y is homogeneous and is assigned an arbitrary label. For the results carried out by pixelwise classifiers, SVM and RF, each pixel is labeled as an ice type or water. The flowchart of the proposed automatic sea-ice mapping system is illustrated in Fig. 3. The system ingests the HH and HV polarized images of the scene, a pretrained pixelwise classifier, and an optional landmask file to neglect the land and image boundary. The pixelwise classifier, which is SVM or RF in this article, is trained using the selected 30 features. Inspired by the mechanism of RF, an energy function $E(k)$ is proposed to obtain l_{R_r} using $\{l_{y_i} | i = 1, 2, \ldots, n_r\}$

$$E(k) = \frac{1}{n_r} \sum_{i=1}^{n_r} \sum_{k=1}^{K} w(k, l_{y_i}) \tag{4}$$

$$w(k, l_{y_i}) = \begin{cases} 0 & l_{y_i} = k \\ 1 & y_{y_i} \neq k \end{cases} \tag{5}$$

$$l_{R_r} = \arg\min\left(E(k)\right) \tag{6}$$

where n_r is the number of pixels in the homogeneous region R_r. w is the weight function and $k \in \{1, 2, \ldots, K\}$ is the class label. When combining the unsupervised segmentation with supervised labeling, all the pixels in the same region share the same label, which is determined as the dominant class according to the pixelwise classification result, with all pixels within it.

TABLE IV
CLASSIFICATION RESULT FOR ALL 18 SCENES

Scene ID	SVM	RF	IRGS-SVM	IRGS-RF
20100418	80.30%	**87.60%**	83.20%	86.10%
20100426	83.40%	88.00%	86.40%	**88.10%**
20100510	85.40%	87.30%	85.90%	**88.00%**
20100524	75.60%	79.00%	85.10%	**86.30%**
20100623	88.10%	**90.80%**	90.20%	90.20%
20100629	70.20%	71.70%	82.40%	**84.10%**
20100721	87.40%	87.40%	85.60%	85.50%
20100730	**78.70%**	73.70%	75.20%	78.10%
20100807	91.90%	93.30%	94.70%	**95.30%**
20100816	86.20%	**86.80%**	85.00%	85.00%
20100907	98.50%	100.00%	100.00%	100.00%
20100909	98.20%	**98.80%**	98.00%	98.00%
20101003	77.70%	77.20%	77.80%	77.70%
20101021	89.40%	90.80%	92.60%	**95.60%**
20101027	65.10%	72.20%	73.00%	**76.90%**
20101114	60.50%	68.80%	65.40%	**75.60%**
20101206	74.90%	83.00%	81.40%	**86.60%**
20101214	69.80%	72.70%	71.80%	**76.90%**
Total	81.13%	83.84%	84.07%	**86.33%**

V. EXPERIMENTS AND ANALYSIS

This study has trained and tested two benchmark classifiers, SVM and RF, and two classifiers based on the proposed framework, IRGS-SVM and IRGS-RF. Both numerical and visual results are presented in this section. The LOO cross-validation strategy is applied to evaluate the robustness and generalization ability of the proposed methods. The classification results of each scene are produced by the classifier that is trained using the rest 17 scenes in the dataset. The cross validation is performed 17 times to ensure no samples from the same scene are employed for both training and test. The overall accuracy based on 500 reference pixels per scene is shown in Table IV. Pixel-based SVM and RF achieved average overall accuracies of 81.13% and 83.84%, respectively. Both SVM and RF struggle when dealing with the freeze-up season. The scene with the worst prediction is on November 14, 2010, with the accuracy of 60.50% and 65.40% executed by SVM and RF, respectively. This scene is the most challenging one in the dataset and will be discussed later in this section. The least challenging scene was acquired on September 7, 2010, when only OW was presented in it.

After integrating with the segmentation results based on the proposed framework, the IRGS-SVM and IRGS-RF achieved average overall accuracies of 84.07% and 86.33%, with improvements of 2.94% and 2.49% compared with pixelwise SVM and RF, respectively. The contribution of the proposed methods can be observed in most scenes in terms of increased classification accuracies. However, the accuracy may decline due to the imbalanced spatial distribution of the SVM and RF results, which the proposed methods adopt as input.

Several studies [27], [50] indicate that conducting incidence angle correction may contribute to higher classification accuracy. Therefore, the improvement of applying incidence angle correction is also investigated in this article. RF and IRGS-RF, which outperform the other two classifiers, are trained and tested

TABLE V
CLASSIFICATION RESULTS BEFORE AND AFTER INCIDENCE ANGLE (IA) CORRECTION FOR RF AND IRGS-RF

Scene ID	RF			IRGS-RF		
	Before IA correction	After IA correction	Difference	Before IA correction	After IA correction	Difference
20100418	87.60%	85.51%	–2.09%	86.10%	85.70%	–0.40%
20100426	88.00%	88.08%	0.08%	88.10%	88.21%	0.11%
20100510	87.30%	87.61%	0.31%	88.00%	88.00%	0.00%
20100524	79.00%	82.53%	3.53%	86.30%	86.30%	0.00%
20100623	90.80%	90.54%	–0.26%	90.20%	90.18%	–0.02%
20100629	71.70%	76.26%	4.56%	84.10%	84.27%	0.17%
20100721	87.40%	86.24%	–1.16%	85.50%	85.34%	–0.16%
20100730	73.70%	76.42%	2.72%	78.10%	78.23%	0.13%
20100807	93.30%	93.48%	0.18%	95.30%	95.28%	–0.02%
20100816	86.80%	83.43%	–3.37%	85.00%	84.91%	–0.09%
20100907	100.00%	100.00%	0.00%	100.00%	100.00%	0.00%
20100909	98.80%	98.47%	–0.33%	98.00%	97.68%	–0.32%
20101003	77.20%	77.06%	–0.14%	77.70%	77.70%	0.00%
20101021	90.80%	92.47%	1.67%	95.60%	95.72%	0.12%
20101027	72.20%	74.64%	2.44%	76.90%	76.90%	0.00%
20101114	68.80%	73.15%	4.35%	75.60%	75.95%	0.35%
20101206	83.00%	86.38%	3.38%	86.60%	87.24%	0.64%
20101214	72.70%	73.28%	0.58%	76.90%	76.90%	0.00%
Total	83.84%	84.75%	0.91%	86.33%	86.36%	0.03%

using the HH/HV scenes calibrated to sigma naught based on the sigma lookup table. Table V gives the comparison of classification accuracy before and after incidence angle correction. The overall accuracy achieved by RF is boosted by 0.91% on the corrected dataset. However, accuracy decline is also observed in several scenes. A potential cause is that the correction may weaken texture patterns for specific GLCM features in the near range. Similar results are reported in [52], [68], and [69]. In contrast, IRGS-RF is robust to incidence angle variation, and improvement by introducing correction is neglectable for all the scenes in terms of classification accuracy. The glocal strategy in IRGS mitigates the effect caused by the incidence angle variation, and the integration mechanism minimizes pixel-level errors caused by outliers in RF results.

The classification results indicate that GLCM features are qualified to distinguish different sea-ice types and water when incorporated with a suitable classifier. Since SVM and RF employ different strategies to solve linearly separable problems, the separability of different sea-ice types and the effectiveness of features that contributed to the classification results are worth investigating. Fig. 5 shows the distributions of GLCM features for different sea-ice types and OW. OW can be efficiently separated from sea ice by some GLCM features, such as ASM and HOM. The distributions of COR for sea ice are highly correlated and are not feasible to discriminate sea-ice types when utilized solely. The distributions of HOM and INV are very similar, indicating information redundancy when using HOM and INV with the same parameters. In agreement with previous research, the results demonstrate that most GLCM features can contribute to the partial separation of OW and different sea-ice types.

The classification results for the April 26, 2010 scene, which was previously shown in Fig. 2 to demonstrate all the steps of the proposed method, is shown in Fig. 6. SVM has been demonstrated as an effective method to classify ice and water, but it does not generate a reasonable ice map in this scene. There are several issues that should be considered when applying pixel-based classifiers. First, the selection of crucial hyperparameters is essential. SVM requires tuned C and gamma, while the number of trees is the only key hyperparameter for RF. More hyperparameters require more computation for grid search and may cause overfitting. Second, SVM uses a kernel function to improve the separability of the features, and the speckle noise in the dataset is more likely to be augmented in the higher dimension. In contrast, the voting and bagging scheme in RF makes it less sensitive to speckle. Fig. 6(e) displays noticeable noise-like errors across the whole scene. Unlike SVM, RF achieves more consistent classification results. According to visual interpretation and ice chart, there is no YI in this scene. However, both SVM and RF misclassified FYI and MYI in the middle right of the scene as YI. On a pixelwise classification level, RF obtains better accuracy compared to SVM. After being combined with the IRGS segmentation result, the noise-like errors are suppressed, and the boundaries are well preserved for both IRGS-SVM and IRGS-RF. Despite that, the improvement of IRGS-RF is negligible in numerical accuracy, because this is validated only on 500 sample points in each scene. The classified image using IRGS-RF is the most visually satisfying among the four methods. IRGS-RF also improves the misclassified YI in the other three scenes. IRGS-RF also improves the misclassified YI area.

After combining unsupervised segmentation with supervised labeling, Both IRGS-SVM and IRGS-RF achieve better classification accuracy, gaining over 2% compared with pixelwise results. The confusion matrices of SVM, IRGS-SVM, RF, and IRGS-RF are shown in Tables VI–IX, respectively. All four classifiers distinguish water from ice with accuracy over 94%. Even with the interference caused by wind and wave, the features are sufficient to describe their characteristics. However, SVM and RF struggle to separate YI from other classes. A possible reason for the misclassified YI may lie in similar backscattering to FYI.

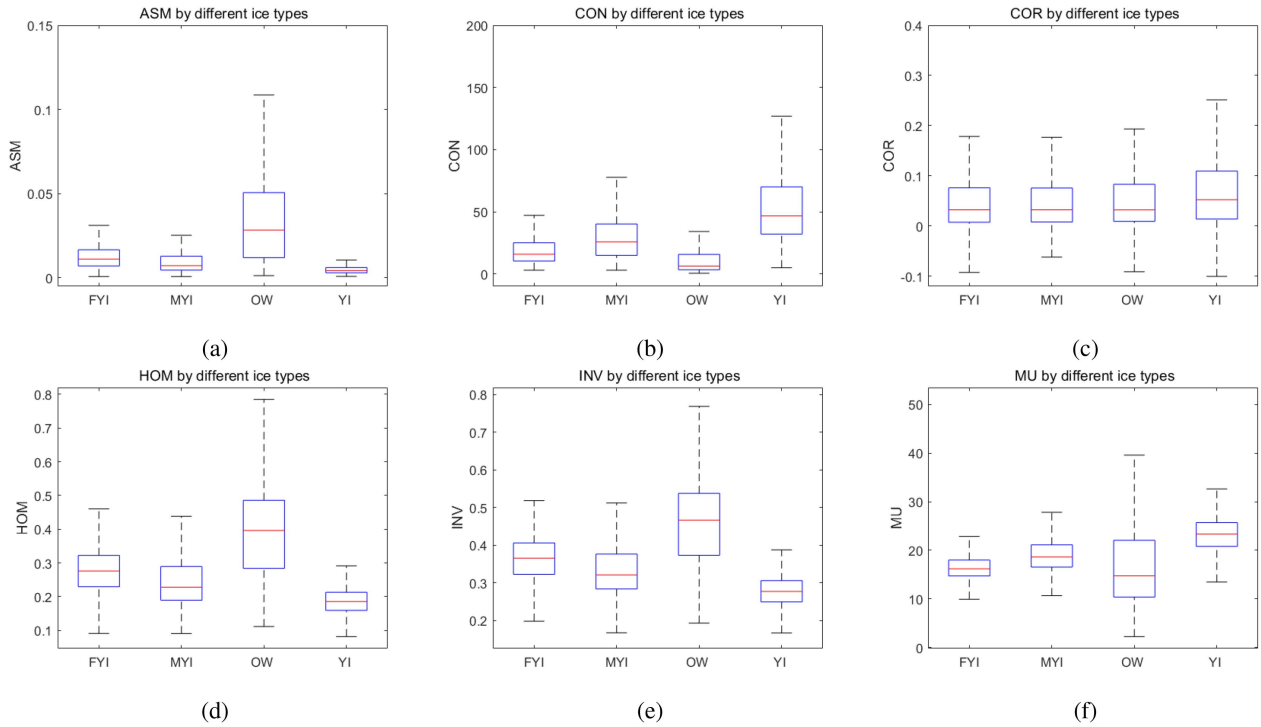

Fig. 5. Distribution of GLCM features for different sea-ice types and OW in box-and-whisker plots. (a) ASM. (b) CON. (c) COR. (d) HOM. (e) INV. (f) MU. All the GLCM features are calculated using a size of 51 with stride of 20.

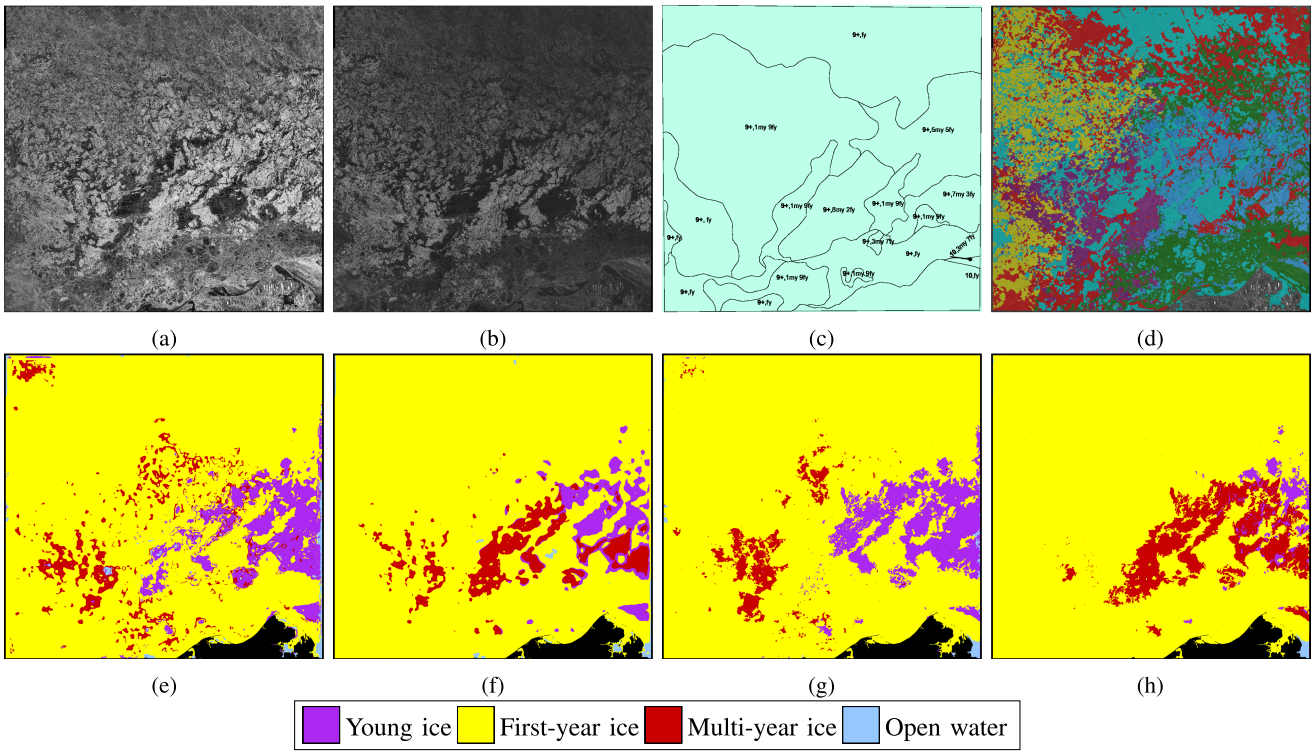

Fig. 6. Classification results of April 26, 2010 (scene ID 20100426). Water (blue), YI (purple), FYI (yellow), and MYI (red). (a) HH polarization. (b) HV polarization. (c) Ice chart. (d) IRGS segmentation result (e) SVM pixel-based classification result with an accuracy of 83.40%. (f) RF pixel-based classification result with an accuracy of 88.00%. (g) IRGS-SVM classification result with an accuracy of 86.40%. (h) IRGS-RF classification result with an accuracy of 88.10%. There should not be YI in this scene according to ice chart. False YI is reduced by combining IRGS result. The final result is more reasonable.

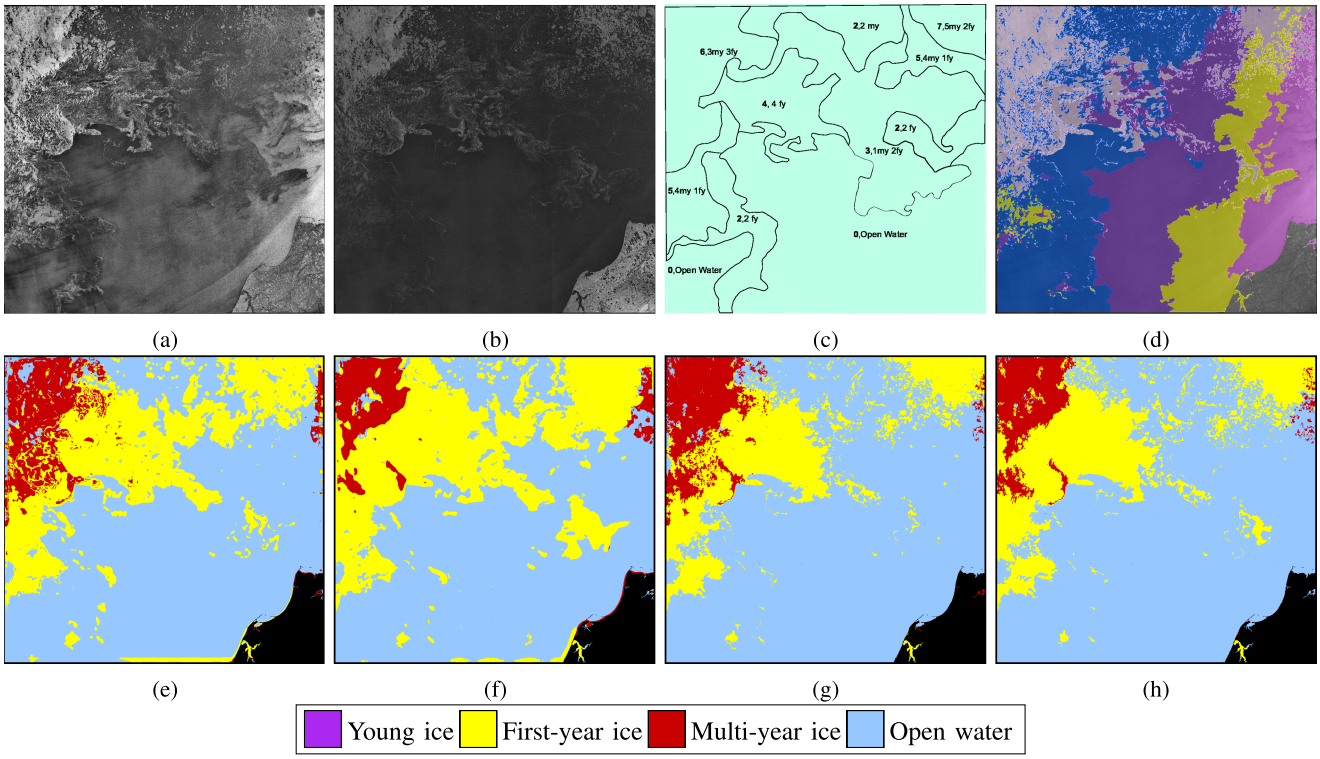

Fig. 7. Classification results of August 7, 2010 (scene ID 20100807). Water (blue), YI (purple), FYI (yellow), and MYI (red). (a) HH polarization. (b) Ice chart. (c) Ice chart. (d) IRGS segmentation result. (e) SVM pixel-based classification result with an accuracy of 91.90%. (f) RF pixel-based classification result with an accuracy of 93.30%. (g) IRGS-SVM classification result with an accuracy of 94.70%. (h) IRGS-RF classification result with an accuracy of 95.30%.

TABLE VI
CLASSIFICATION CONFUSION MATRIX OF SVM

	YI	FYI	MYI	OW
YI	**44.86%**	40.50%	4.29%	10.35%
FYI	5.16%	**85.27%**	4.12%	5.46%
MYI	16.56%	5.46%	**70.25%**	7.73%
OW	0.50%	4.72%	0.02%	**94.76%**

TABLE VII
CLASSIFICATION CONFUSION MATRIX OF RF

	YI	FYI	MYI	OW
YI	**57.52%**	34.45%	5.17%	2.86%
FYI	3.97%	**87.68%**	2.61%	5.74%
MYI	13.47%	13.28%	**72.07%**	1.18%
OW	1.18%	4.60%	0.06%	**94.16%**

TABLE VIII
CLASSIFICATION CONFUSION MATRIX OF IRGS-SVM

	YI	FYI	MYI	OW
YI	**58.747%**	29.17%	0.48%	11.62%
FYI	3.06%	**91.16%**	1.53%	4.25%
MYI	13.58%	2.46%	**77.30%**	6.65%
OW	0.49%	4.98%	0.00%	**94.53%**

TABLE IX
CLASSIFICATION CONFUSION MATRIX OF IRGS-RF

	YI	FYI	MYI	OW
YI	**70.77%**	22.74%	3.21%	3.28%
FYI	2.56%	**91.92%**	1.79%	3.74%
MYI	8.20%	10.03%	**78.85%**	2.92%
OW	0.67%	4.84%	0.03%	**94.46%**

34.45% of YI is categorized as FYI by RF. YI only appears in five scenes in the dataset, covering from late October through December. The limited labeled samples may cause the poor performance of classifying YI. Although pixel-based classifiers do not achieve satisfactory results, the proposed IRGS-SVM and IRGS-RF are able to boost the classification accuracy and present visual-appealing sea-ice maps.

Mapping sea ice during the summer melting season is usually tricky. The melting reduces the surface roughness of ice and degrades the texture captured by backscatter. The melting ponds presented onsite also change the electromagnetic characteristics of the ice beneath. An example scene obtained on August 7, 2010 is depicted in Fig. 7. It is a complex scene that contains FYI, MYI, and OW. All four models distinguish the OW in the lower part of the scene. Although water around the image boundary is misclassified as FYI by pixelwise SVM and RF, these errors are effectively mitigated by the combined models, IRGS-SVM and IRGS-RF. The upper part is more challenging since the surface roughness of sea ice is reduced by melting. Different types of ice show a very similar texture to OW in this scene, leading to confusion when discriminating OW and sea-ice types. Therefore, the presence of FYI is overstated by SVM and RF. The proposed IRGS-RF is robust to these FYI errors and achieves higher classification accuracy of 95.30%. Most MYI floes in the upper right corner are also preserved in the results.

The classification result of October 21, 2010 is displayed in Fig. 8. The gray ice appearing in the top left corner has a much lower backscattering level than other gray ice displayed in the

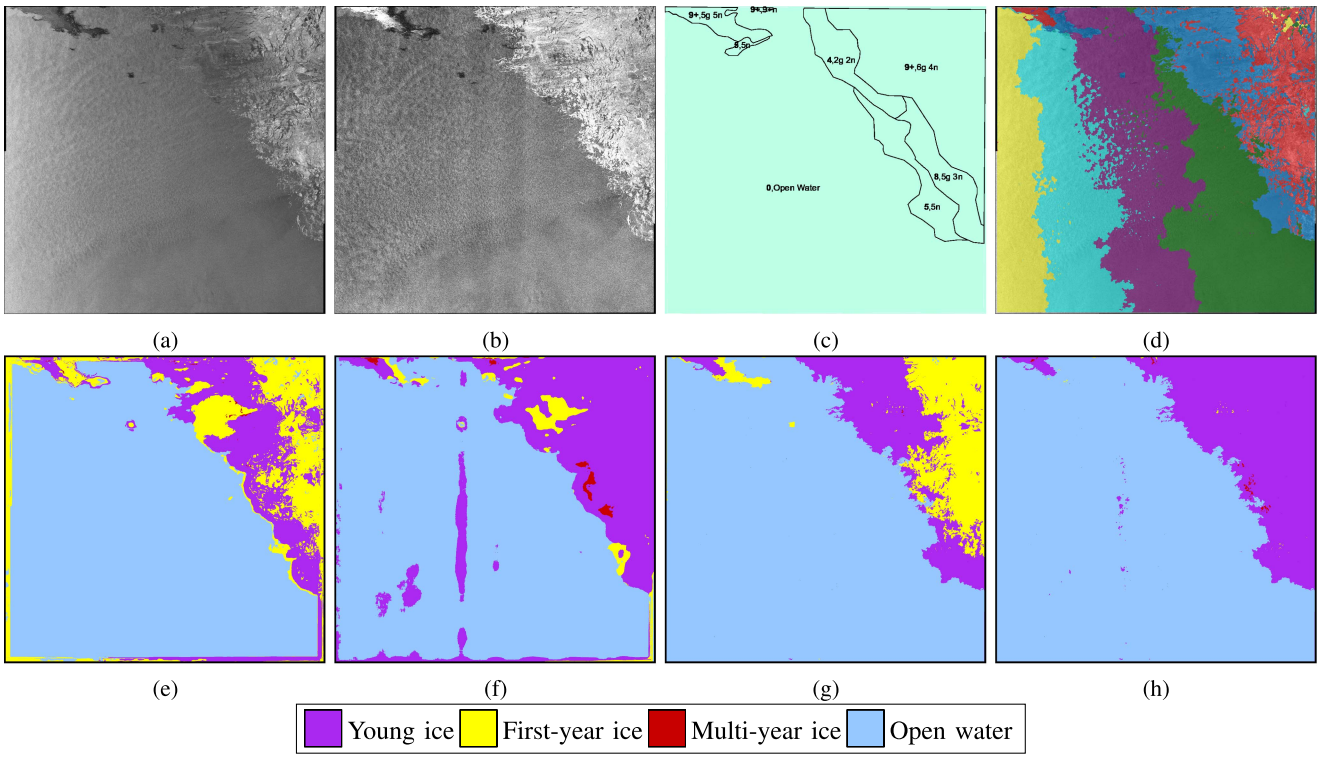

Fig. 8. Classification results of October 21, 2010 (scene ID 20101021). Water (blue), YI (purple), FYI (yellow), and MYI (red). (a) HH polarization. (b) HV polarization. (c) Ice chart. (d) IRGS segmentation result. (e) SVM pixel-based classification result with an accuracy of 89.40%. (f) RF pixel-based classification result with an accuracy of 90.80%. (g) IRGS-SVM classification result with an accuracy of 92.60%. (h) IRGS-RF classification result with an accuracy of 95.60%.

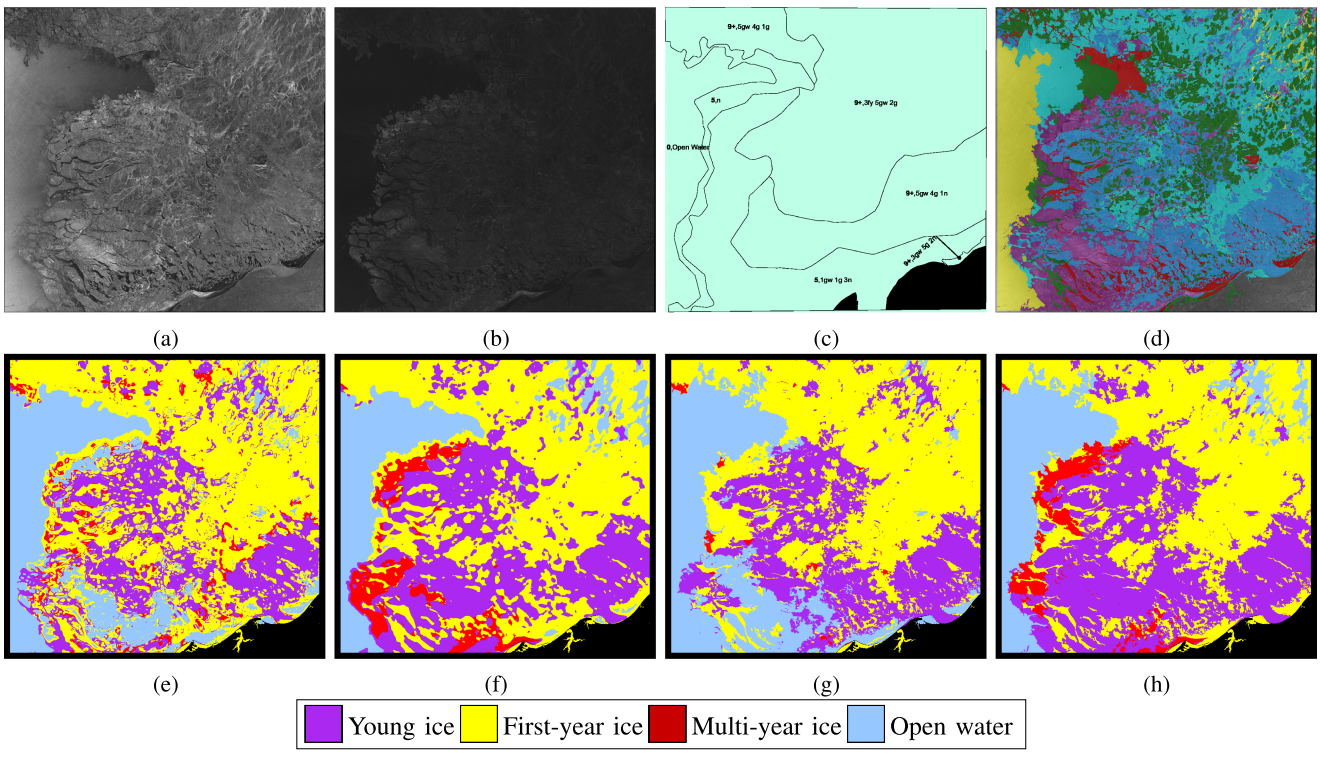

Fig. 9. Classification results of November 14, 2010 (scene ID 20101114). Water (blue), YI (purple), FYI (yellow), and MYI (red). (a) HH polarization. (b) Ice chart. (c) Ice chart. (d) IRGS segmentation result. (e) SVM pixel-based classification result with an accuracy of 60.50%. (f) RF pixel-based classification result with an accuracy of 68.80%. (g) IRGS-SVM classification result with an accuracy of 65.40%. (h) IRGS-RF classification result with an accuracy of 75.60%.

scene. Another challenge presented is the noticeable banding artifacts in the middle of the HV scene. The dataset is collected under ScanSAR wide beam mode, and adjoining multiple scan beams cause these vertical bands. Since HV polarization has a much lower signal-to-noise ratio, the banding artifacts are quite common in the HV scene. SVM and IRGS-SVM do not get affected by banding artifacts. However, there is no FYI in this scene, and SVM and IRGS-SVM misclassify YI as FYI. RF obtains much better results compared to SVM. Although the banding artifacts greatly impact the pixelwise RF result, the combination with segmentation almost resolves this issue, leaving only a small error on the IRGS-RF result.

Fig. 9 (November 14 2010) represents the most challenging scene with different ice types and water. The proposed IRGS+RF achieves the lowest accuracy of 75.60% of all 18 scenes. First, the incidence angle effect is significant in the scene. The backscattering signature is inconsistent across the whole image—the left of the scene is brighter than the right side. Second, given the 200 m $\times$ 200 m pixel size, a single pixel may contain several types of ice and water. The pixelwise classifiers struggle to distinguish these mixed pixels. Third, there are numerous leads presented among sea ice in this scene. These leads may have generated misleading texture features that confused the classifiers. Although the pixelwise results are unsatisfying, the combined methods suppress these phenomena and achieve higher classification accuracy and natural boundaries between different ice types and water.

The experiments are run on a computer with the following configuration: Intel Core i5-6600K, 16-GB RAM, Windows 10 operating system. The average execution time to generate a sea-ice map based on a RADARSAT-2 scene is less than 25 min. Specifically, it takes 3 min to oversegment the scene into homogeneous regions. The GLCM feature extraction, as the most time-consuming part of the workflow, takes around 15 min. SVM takes 5 min for pixelwise labeling, while RF only takes 20 s credited to parallel computing. The proposed system is qualified to deploy on business computers with average configurations and classify sea ice in a scene within half an hour.

VI. Conclusion

An automatic sea-ice classification system using RADARSAT-2 SAR imagery is proposed in this article. To the best of the authors' knowledge, this is the first study combining segmentation with pixelwise labeling, using an energy function, to classify different sea-ice types. The unsupervised IRGS segmentation algorithm extracts spatial contextual information in the SAR scene to divide the whole image into homogeneous regions, while the pixelwise classifier exploits backscatter intensities and textural features to label each region. Two benchmark pixelwise classifiers, SVM and RF, and two proposed models, IRGS-SVM and IRGS-RF, were trained and tested on a dataset to find the best combination for building the system.

To better evaluate the proposed models, a dataset consisting of 18 RADARSAT-2 scenes of the Beaufort Sea is used to evaluate the proposed models. The dataset includes scenes from melting, summer, and freezing seasons. The LOO strategy is applied for cross validation to avoid using samples from the same scene for both training and testing. The results show that the proposed models achieve an overall accuracy of 86.33% on the dataset and are robust to melting season, which is the most challenging period of the year.

When only applying pixelwise classifiers, RF obtains an overall accuracy of 84.07% compared to 81.13% by SVM. Comparing the visual results, the sea-ice maps generated by RF contain fewer noise-like errors than SVM. In general, RF outperforms SVM on most of the scenes in the dataset, indicating that RF is a more reliable choice when dealing with sea-ice classification based on texture features. After combining IRGS segmentation results with the pixel-level labels, the classification accuracies of IRGS-SVM and IRGS-RF are both improved. IRGS-RF achieves the best performance with an 86.33% success rate for distinguishing ice types and water.

Moreover, experiments are conducted on calibrated SAR data to evaluate the robustness of the proposed method. The classification accuracies of RF are boosted for most scenes using the SAR imagery calibrated to sigma naught. However, IRGS-RF achieves almost identical overall accuracies on both calibrated and uncalibrated data because the integration mechanism in IRGS-RF minimizes pixel-level errors caused by outliers in RF results. The results indicate that the proposed method is robust to the incidence angle variation in dual-pol SAR data.

The novel sea-ice classification method not only achieves promising classification results, but also produces visually appealing ice maps. The boundaries between water and different ice types are well preserved, and the pixel-level errors are refined. The final sea-ice maps are highly consistent with the CIS's ice charts. Analysts can apply these automatically generated maps as references for sea-ice interpretation in the operational pipeline at ice services. The proposed model will be tested on dataset with different temporal and spatial distributions using transfer learning in future work. The significance of applying noise floor correction will be explored. The effect of utilizing information of neighboring segments to improve the sea-ice classification performance will also be investigated.

References

[1] N. Zakhvatkina, A. Korosov, S. Muckenhuber, S. Sandven, and M. Babiker, "Operational algorithm for ice–water classification on dual-polarized RADARSAT-2 images," *Cryosphere*, vol. 11, no. 1, pp. 33–46, 2017.

[2] L. P. Bobylev and M. W. Miles, "Sea ice in the arctic paleoenvironments," in *Sea Ice in the Arctic*. New York, NY, USA: Springer, 2020, pp. 9–56.

[3] Joint WMO-IOC Technical Commission for Oceanography and Marine Meteorology, "Ice chart colour code standard, version 1.0, 2014," World Meteorological Organization & Intergovernmental Oceanographic Commission, Geneva, Switzerland, *Tech. Rep. WMO TD: 1215b*, 2014.

[4] Interpreting ice charts, 2016. [Online]. Available: https://www.canada.ca/en/environment-climate-change/services/ice-forecasts-observations/publications/interpreting-charts.html

[5] Q. Yu, "Automated SAR sea ice interpretation," Ph.D. dissertation, Dept. Syst. Des. Eng., Univ. Waterloo, Waterloo, ON, Canada, 2006.

[6] B. Scheuchl, D. Flett, R. Caves, and I. Cumming, "Potential of RADARSAT-2 data for operational sea ice monitoring," *Can. J. Remote Sens.*, vol. 30, no. 3, pp. 448–461, 2004.

[7] A. A. Thompson*, "Overview of the RADARSAT constellation mission," *Can. J. Remote Sens.*, vol. 41, no. 5, pp. 401–407, 2015.

[8] S. Khaleghian, H. Ullah, T. Kræmer, N. Hughes, T. Eltoft, and A. Marinoni, "Sea ice classification of SAR imagery based on convolution neural networks," *Remote Sens.*, vol. 13, no. 9, 2021, Art. no. 1734.

[9] S. Khaleghian, H. Ullah, T. Krmer, T. Eltoft, and A. Marinoni, "Deep semi-supervised teacher-student model based on label propagation for sea ice classification," *IEEE J. Sel. Topics Appl. Earth Observ. Remote Sens.*, vol. 14, pp. 10761–10772, 2021.

[10] L. Zhang, H. Liu, X. Gu, H. Guo, J. Chen, and G. Liu, "Sea ice classification using TerraSAR-X ScanSAR data with removal of scalloping and interscan banding," *IEEE J. Sel. Topics Appl. Earth Observ. Remote Sens.*, vol. 12, no. 2, pp. 589–598, Feb. 2019.

[11] B. Scheuchl, R. Caves, D. Flett, R. De Abreu, M. Arkett, and I. Cumming, "The potential of cross-polarization information for operational sea ice monitoring," in *Proc. Envisat ERS Symp.*, vol. 572, 2005, pp. 1–7.

[12] K. D. Ward, S. Watts, and R. J. Tough, *Sea Clutter: Scattering, The K Distribution and Radar Performance*. Stevenage, U.K.: Inst. Eng. Technol., 2006.

[13] M. Mäkynen and M. Hallikainen, "Investigation of C- and X-band backscattering signatures of Baltic sea ice," *Int. J. Remote Sens.*, vol. 25, no. 11, pp. 2061–2086, 2004.

[14] W. Dierking, "Mapping of different sea ice regimes using images from Sentinel-1 and ALOS synthetic aperture radar," *IEEE Trans. Geosci. Remote Sens.*, vol. 48, no. 3, pp. 1045–1058, Mar. 2010.

[15] J. P. Gill and J. J. Yackel, "Evaluation of C-band SAR polarimetric parameters for discrimination of first-year sea ice types," *Can. J. Remote Sens.*, vol. 38, no. 3, pp. 306–323, 2012.

[16] S. Singha, M. Johansson, N. Hughes, S. M. Hvidegaard, and H. Skourup, "Arctic sea ice characterization using spaceborne fully polarimetric L-, C-, and X-band SAR with validation by airborne measurements," *IEEE Trans. Geosci. Remote Sens.*, vol. 56, no. 7, pp. 3715–3734, Jul. 2018.

[17] L. He, X. He, F. Hui, Y. Ye, T. Zhang, and X. Cheng, "Investigation of polarimetric decomposition for Arctic summer sea ice classification using Gaofen-3 fully polarimetric SAR data," *IEEE J. Sel. Topics Appl. Earth Observ. Remote Sens.*, vol. 15, pp. 3904–3915, 2022.

[18] M. Dabboor and M. Shokr, "Assessment of compact polarimetric SAR parameters for lake and fast sea ice characterization," in *Proc. IEEE Int. Geosci. Remote Sens. Symp.*, 2019, pp. 5840–5842.

[19] J. Karvonen, "Virtual radar ice buoys—A method for measuring fine-scale sea ice drift," *Cryosphere*, vol. 10, no. 1, pp. 29–42, 2016.

[20] J. Lehtiranta, S. Siiriä, and J. Karvonen, "Comparing C-and L-band SAR images for sea ice motion estimation," *Cryosphere*, vol. 9, no. 1, pp. 357–366, 2015.

[21] D. Murashkin, G. Spreen, M. Huntemann, and W. Dierking, "Method for detection of leads from Sentinel-1 SAR images," *Ann. Glaciol.*, vol. 59, pp. 124–136, 2018.

[22] D. A. Clausi, "An analysis of co-occurrence texture statistics as a function of grey level quantization," *Can. J. Remote Sens.*, vol. 28, no. 1, pp. 45–62, 2002.

[23] H. Liu, H. Guo, X.-M. Li, and L. Zhang, "An approach to discrimination of sea ice from open water using SAR data," in *Proc. IEEE Int. Geosci. Remote Sens. Symp.*, 2016, pp. 4865–4867.

[24] H. Su, Y. Wang, J. Xiao, and X.-H. Yan, "Classification of MODIS images combining surface temperature and texture features using the support vector machine method for estimation of the extent of sea ice in the frozen Bohai Bay, China," *Int. J. Remote Sens.*, vol. 36, no. 10, pp. 2734–2750, 2015.

[25] W. Tan, "Sea ice mapping in Labrador coast with Sentinel-1 synthetic aperture radar imagery," master's thesis, Dept. Geogr. Environ. Manage., Univ. Waterloo, Waterloo, ON, Canada, 2017.

[26] M. S. Mahmud, V. Nandan, S. E. Howell, T. Geldsetzer, and J. Yackel, "Seasonal evolution of L-band SAR backscatter over landfast Arctic sea ice," *Remote Sens. Environ.*, vol. 251, 2020, Art. no. 112049.

[27] S. Singha, A. M. Johansson, and A. P. Doulgeris, "Robustness of SAR sea ice type classification across incidence angles and seasons at L-band," *IEEE Trans. Geosci. Remote Sens.*, vol. 59, no. 12, pp. 9941–9952, Dec. 2020.

[28] M. Dabboor, B. Montpetit, S. Howell, and C. Haas, "Improving sea ice characterization in dry ice winter conditions using polarimetric parameters from C-and L-band SAR data," *Remote Sens.*, vol. 9, no. 12, 2017, Art. no. 1270.

[29] M. S. Mahmud, T. Geldsetzer, S. E. L. Howell, J. J. Yackel, V. Nandan, and R. K. Scharien, "Incidence angle dependence of HH-polarized C- and L-band wintertime backscatter over Arctic sea ice," *IEEE Trans. Geosci. Remote Sens.*, vol. 56, no. 11, pp. 6686–6698, Nov. 2018.

[30] M.-A. Moen et al., "Comparison of feature based segmentation of full polarimetric SAR satellite sea ice images with manually drawn ice charts," *Cryosphere*, vol. 7, no. 6, pp. 1693–1705, 2013.

[31] A. Y. Ng and M. I. Jordan, "On discriminative vs. generative classifiers: A comparison of logistic regression and naive Bayes," in *Proc. Int. Conf. Neural Inf. Process. Syst.*, 2002, pp. 841–848.

[32] H. Liu, H. Guo, and L. Zhang, "SVM-based sea ice classification using textural features and concentration from RADARSAT-2 dual-pol ScanSAR data," *IEEE J. Sel. Topics Appl. Earth Observ. Remote Sens.*, vol. 8, no. 4, pp. 1601–1613, Apr. 2015.

[33] J. Lohse, A. P. Doulgeris, and W. Dierking, "An optimal decision-tree design strategy and its application to sea ice classification from SAR imagery," *Remote Sens.*, vol. 11, no. 13, 2019, Art. no. 1574.

[34] H. Han et al., "Retrieval of melt ponds on Arctic multiyear sea ice in summer from TerraSAR-X dual-polarization data using machine learning approaches: A case study in the chukchi sea with mid-incidence angle data," *Remote Sens.*, vol. 8, no. 1, 2016, Art. no. 57.

[35] A. Gegiuc, M. Similä, J. Karvonen, M. Lensu, M. Mäkynen, and J. Vainio, "Estimation of degree of sea ice ridging based on dual-polarized C-band SAR data," *Cryosphere*, vol. 12, no. 1, pp. 343–364, 2018.

[36] E. Maggiori, Y. Tarabalka, G. Charpiat, and P. Alliez, "Convolutional neural networks for large-scale remote-sensing image classification," *IEEE Trans. Geosci. Remote Sens.*, vol. 55, no. 2, pp. 645–657, Feb. 2017.

[37] R. Ressel, A. Frost, and S. Lehner, "A neural network-based classification for sea ice types on X-band SAR images," *IEEE J. Sel. Topics Appl. Earth Observ. Remote Sens.*, vol. 8, no. 7, pp. 3672–3680, Jul. 2015.

[38] W. Song et al., "Automatic sea-ice classification of SAR images based on spatial and temporal features learning," *IEEE Trans. Geosci. Remote Sens.*, vol. 59, no. 12, pp. 9887–9901, Dec. 2021.

[39] H. Boulze, A. Korosov, and J. Brajard, "Classification of sea ice types in Sentinel-1 SAR data using convolutional neural networks," *Remote Sens.*, vol. 12, no. 13, 2020, Art. no. 2165.

[40] W. Song, M. Li, Q. He, D. Huang, C. Perra, and A. Liotta, "A residual convolution neural network for sea ice classification with Sentinel-1 SAR imagery," in *Proc. IEEE Int. Conf. Data Mining Workshops*, 2018, pp. 795–802.

[41] Y. Ren, H. Xu, B. Liu, and X. Li, "Sea ice and open water classification of SAR images using a deep learning model," in *Proc. IEEE Int. Geosci. Remote Sens. Symp.*, 2020, pp. 3051–3054.

[42] R. Jobanputra and D. A. Clausi, "Preserving boundaries for image texture segmentation using grey level co-occurring probabilities," *Pattern Recognit.*, vol. 39, no. 2, pp. 234–245, 2006.

[43] T. Zhu, F. Li, G. Heygster, and S. Zhang, "Antarctic sea-ice classification based on conditional random fields from RADARSAT-2 dual-polarization satellite images," *IEEE J. Sel. Topics Appl. Earth Observ. Remote Sens.*, vol. 9, no. 6, pp. 2451–2467, Jun. 2016.

[44] R. Ressel, S. Singha, S. Lehner, A. Rösel, and G. Spreen, "Investigation into different polarimetric features for sea ice classification using X-band synthetic aperture radar," *IEEE J. Sel. Topics Appl. Earth Observ. Remote Sens.*, vol. 9, no. 7, pp. 3131–3143, Jul. 2016.

[45] M. Dabboor, B. Montpetit, and S. Howell, "Assessment of the high resolution SAR mode of the RADARSAT constellation mission for first year ice and multiyear ice characterization," *Remote Sens.*, vol. 10, no. 4, 2018, Art. no. 594.

[46] Y. Zhang et al., "Sea ice and water classification on dual-polarized Sentinel-1 imagery during melting season," *Cryosphere Discussions*, vol. 2021, pp. 1–26, 2021.

[47] S. Ochilov and D. A. Clausi, "Operational SAR sea-ice image classification," *IEEE Trans. Geosci. Remote Sens.*, vol. 50, no. 11, pp. 4397–4408, Nov. 2012.

[48] S. Leigh, Z. Wang, and D. A. Clausi, "Automated ice–water classification using dual polarization SAR satellite imagery," *IEEE Trans. Geosci. Remote Sens.*, vol. 52, no. 9, pp. 5529–5539, Sep. 2014.

[49] R. G. Onstott and F. Carsey, "SAR and scatterometer signatures of sea ice," *Microw. Remote Sens. Sea Ice*, vol. 68, pp. 73–104, 1992.

[50] J. Lohse, A. P. Doulgeris, and W. Dierking, "Mapping sea-ice types from Sentinel-1 considering the surface-type dependent effect of incidence angle," *Ann. Glaciol.*, vol. 61, no. 83, pp. 260–270, 2020.

[51] M. Mäkynen and J. Karvonen, "Incidence angle dependence of first-year sea ice backscattering coefficient in Sentinel-1 SAR imagery over the Kara sea," *IEEE Trans. Geosci. Remote Sens.*, vol. 55, no. 11, pp. 6170–6181, Nov. 2017.

[52] A. S. Komarov and M. Buehner, "Detection of first-year and multi-year sea ice from dual-polarization SAR images under cold conditions," *IEEE Trans. Geosci. Remote Sens.*, vol. 57, no. 11, pp. 9109–9123, Nov. 2019.

[53] Joint WMO-IOC Technical Commission for Oceanography and Marine Meteorology, "Sea ice nomenclature," World Meteorological Organization & Intergovernmental Oceanographic Commission, volume 1—Terminology and Codes, Volume II—Illustrated Glossary and III—International System of Sea-Ice Symbols, Geneva, Switzerland, Tech. Rep. WMO No 259, 2014.
[54] Q. Yu and D. A. Clausi, "SAR sea-ice image analysis based on iterative region growing using semantics," *IEEE Trans. Geosci. Remote Sens.*, vol. 45, no. 12, pp. 3919–3931, Dec. 2007.
[55] D. Clausi, A. Qin, M. Chowdhury, P. Yu, and P. Maillard, "MAGIC: MAP-guided ice classification system," *Can. J. Remote Sens.*, vol. 36, pp. S13–S25, 2010.
[56] L. Vincent and P. Soille, "Watersheds in digital spaces: An efficient algorithm based on immersion simulations," *IEEE Trans. Pattern Anal. Mach. Intell.*, vol. 13, no. 6, pp. 583–598, Jun. 1991.
[57] J. Wang, C. Duguay, D. Clausi, V. Pinard, and S. Howell, "Semi-automated classification of lake ice cover using dual polarization RADARSAT-2 imagery," *Remote Sens.*, vol. 10, no. 11, 2018, Art. no. 1727.
[58] Q. Yu and D. A. Clausi, "IRGS: Image segmentation using edge penalties and region growing," *IEEE Trans. Pattern Anal. Mach. Intell.*, vol. 30, no. 12, pp. 2126–2139, Dec. 2008.
[59] D. Barber and E. LeDrew, "SAR sea ice discrimination using texture statistics—A multivariate approach," *Photogrammetric Eng. Remote Sens.*, vol. 57, no. 4, pp. 385–395, 1991.
[60] J. H. Friedman, "On bias, variance, 0/1-loss, and the curse-of-dimensionality," *Data Mining Knowl. Discov.*, vol. 1, no. 1, pp. 55–77, 1997.
[61] M. Verleysen and D. François, "The curse of dimensionality in data mining and time series prediction," in *Proc. Int. Work-Conf. Artif. Neural Netw.*, 2005, pp. 758–770.
[62] P. M. Granitto, C. Furlanello, F. Biasioli, and F. Gasperi, "Recursive feature elimination with random forest for PTR-MS analysis of agroindustrial products," *Chemometrics Intell. Lab. Syst.*, vol. 83, no. 2, pp. 83–90, 2006.
[63] L. Xu, J. Li, and A. Brenning, "A comparative study of different classification techniques for marine oil spill identification using RADARSAT-1 imagery," *Remote Sens. Environ.*, vol. 141, pp. 14–23, 2014.
[64] G. S. Chavan, S. Manjare, P. Hegde, and A. Sankhe, "A survey of various machine learning techniques for text classification," *Int. J. Eng. Trends Technol.*, vol. 15, no. 6, pp. 288–292, 2014.
[65] T. K. Ho, "The random subspace method for constructing decision forests," *IEEE Trans. Pattern Anal. Mach. Intell.*, vol. 20, no. 8, pp. 832–844, Aug. 1998.
[66] R. Shrivastava, H. Mahalingam, and N. Dutta, "Application and evaluation of random forest classifier technique for fault detection in bioreactor operation," *Chem. Eng. Commun.*, vol. 204, no. 5, pp. 591–598, 2017.
[67] L. Breiman, "Random forests," *Mach. Learn.*, vol. 45, no. 1, pp. 5–32, 2001.
[68] L. Wang, K. A. Scott, and D. A. Clausi, "Sea ice concentration estimation during freeze-up from SAR imagery using a convolutional neural network," *Remote Sens.*, vol. 9, no. 5, 2017, Art. no. 408.
[69] J. Lohse, A. P. Doulgeris, and W. Dierking, "Incident angle dependence of Sentinel-1 texture features for sea ice classification," *Remote Sens.*, vol. 13, no. 4, 2021, Art. no. 552.

Mingzhe Jiang (Student Member, IEEE) received the B.Eng. degree in electronic information engineering and the M.Eng. degree in signal and information processing from the Hefei University of Technology, Hefei, China, in 2013 and 2016, respectively. He is currently working toward the Ph.D. degree in systems design engineering with the University of Waterloo, Waterloo, ON, Canada.

His research interests include machine learning and image processing with applications in remote sensing.

David A. Clausi (Senior Member, IEEE) received the Ph.D. degree in systems design engineering from the University of Waterloo, Waterloo, ON, Canada, in 1996.

He then worked in medical imaging with Mitra Imaging, Waterloo. He started his academic career in 1997 as an Assistant Professor in Geomatics Engineering with the University of Calgary, Calgary, AB, Canada. In 1999, he returned to the University of Waterloo, where he is currently a Professor and specializes in the field of intelligent systems and is the Associate Dean Research and External Partnerships with the Faculty of Engineering. He has many contributions, conducting research primarily in remote sensing, computer vision, image processing, and algorithm design. He has published extensively, received many scholarships, paper awards, research awards, and teaching excellence awards, and his efforts have led to successful commercial implementations, culminating in the creation, and sale of a tech company.

Dr. Clausi was the Co-Chair of the International Association for Pattern Recognition Technical Committee 7—Remote Sensing from 2004 to 2006. He is a Fellow of the Canadian Academy of Engineering.

Linlin Xu (Member, IEEE) received the B.Eng. and M.Sc. degrees in geomatics engineering from the China University of Geosciences, Beijing, China, in 2007 and 2010, respectively, and the Ph.D. degree in remote sensing from the Department of Geography and Environmental Management, University of Waterloo, Waterloo, ON, Canada, in 2014.

He has authored or coauthored various papers in high-impact remote sensing journals and conferences. His research interests include machine learning, remote sensing, and environmental monitoring.